

# Influence of strongly-constrained liquid-filled composite armor on stability of incoming shaped charge jet during eccentric penetration

You-er Cai<sup>a</sup> , Zhengxiang Huang<sup>a\*</sup> , Yaping Tan<sup>a</sup> , Xudong Zu<sup>a</sup> , Xiaojun Shen<sup>a,b</sup> , Xin Jia<sup>a</sup> 

<sup>a</sup>School of Mechanical Engineering, Nanjing University of Science and Technology, Nanjing 210094, China. Email: caiyouer@njust.edu.cn, huangyue@njust.edu.cn, 315101002424@njust.edu.cn, zuxudong9902@njust.edu.cn, sxj\_1959@126.com, jjaxin@mail.njust.edu.cn

<sup>b</sup>Unit 63961 Peoples Liberation Army 6th Beiyuan Road, Chaoyang Beijing, 10012, China.

\* Corresponding author

<https://doi.org/10.1590/1679-78257098>

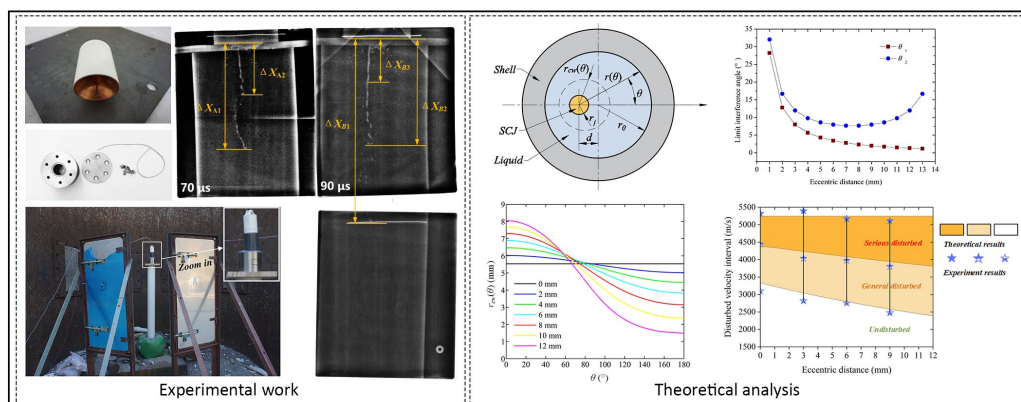
## Abstract

Compared with central penetration, the eccentric penetration of jet into a liquid-filled composite armor (LCA) shows a more obvious lateral displacement due to the asymmetric impact by the shock wave and liquid radial reflux. Based on this characteristic, the reaming process in the liquid layer during the shaped charge jet (SCJ) penetrates into the strongly-constrained liquid-filled composite armor (SLCA) eccentrically, the interference process of jet is subjected to the asymmetric impact by the shock wave and liquid radial reflux, and the lateral movement process of the SCJ under lateral force loading is analyzed to study the influence of SLCA on the stability of incoming SCJ during eccentric penetration. Theoretical and X-ray experimental results show that when the eccentricity distance is [0 mm, 12 mm], the severely disturbed velocity range and total disturbed velocity range of the SCJ increase with the increase of the eccentricity distance, while the maximum lateral displacement of the SCJ decreases slightly with the increase of the eccentricity distance at [1 mm, 12 mm].

## Keywords

Liquid-filled composite armor, shaped charge jet, eccentric penetration, asymmetric impact.

## Graphical Abstract



Received: April 28, 2022. In revised form May 05, 2022. Accepted May 12, 2022. Available online: May 16, 2022.

<https://doi.org/10.1590/1679-78257098>

 Latin American Journal of Solids and Structures. ISSN 1679-7825. Copyright © 2022. This is an Open Access article distributed under the terms of the [Creative Commons Attribution License](https://creativecommons.org/licenses/by/4.0/), which permits unrestricted use, distribution, and reproduction in any medium, provided the original work is properly cited.

## 1 INTRODUCTION

With the increasing firepower of modern weapons, the safety of a mobile launching platform of weapons such as tanks and ships is increasingly threatened. Among them, high speed shaped charge jet (SCJ) produced by APHE is one of the main threats faced by mobile platforms and personnel in the battlefield. According to existing research, the penetration ability of SCJ can reach more than 10 times caliber, so the protection of SCJ has become one of the key research points in the field of impact protection.

Liquid-filled composite armor (LCA), a new type of protective armor, has gradually attracted the attention of scholars in impact protection. The protective mechanism of LCA is different from that of other passive protective devices. It interferes with SCJ by means of shock wave propagation and liquid radial reflux, and plays a role in generating rigidity with softness. The process of SCJ penetration into LCA is shown in Figure 1, which can be roughly divided into four stages: jet penetration into cover plate, jet reaming in liquid, jet disturbed by shock wave impact and liquid radial reflux, jet penetration into bottom plate and liquid spraying. After penetrating the LCA, the tip and middle section of the SCJ is seriously disturbed, which leads to fracture and lateral movement, and the residual penetration capability is greatly reduced.

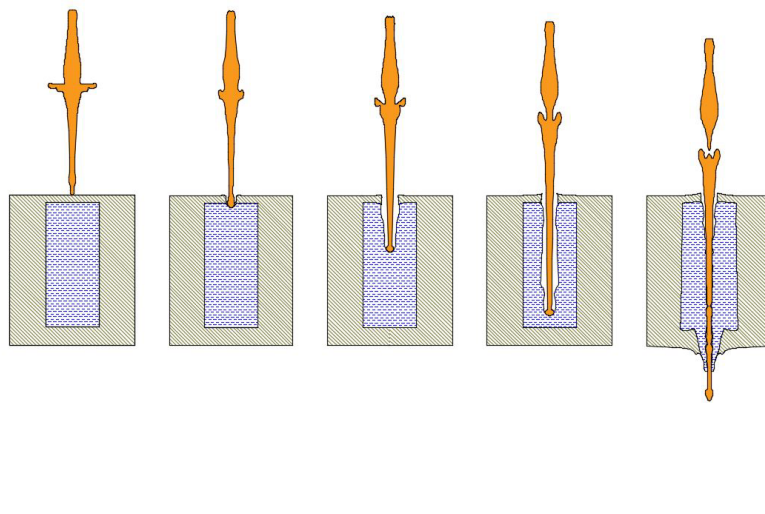


**Figure 1** Schematic of jet penetration into liquid-filled composite armor

To date, many relevant studies have been conducted on the interaction between kinetic energy penetrators such as high-speed projectiles and fragments and liquid-containing vessels by Truscott et al. (2014), Lundstrom and Fung (1976) and Lundstrom (1988), Lee et al. (1996 & 1997), Thomas et al. (2014) and Fourest et al. (2015), mainly focusing on the water hammer effect caused by kinetic energy penetrators penetrating into liquid-containing vessels such as aircraft and tanks. Studies include the description of liquid cavity shape, calculation of water spray, analysis of pressure change in liquid, and so on. Some relevant studies have also been conducted on the jet penetration process in liquid, among which Held and Backofen (1990) studied the penetration behavior of copper, aluminum and tantalum molding jets in water by using high-speed photography and intermittent switch technology. Lee et al. (1995) studied the penetration process of jet particles in water through high-speed photography and X-ray experiment. Held (1995) and Held et al. (1996) slightly improved the Szendrei equation and measured the radial crater growing process of jet penetration into water with high space and time resolution by using the profile streak technique.

In recent years, scholars have conducted studies on the process of jet penetration into liquid-containing containers, but few articles have been published. White and Wahll (1981) studied the process of jet penetration into an airtight structure full of water or other liquids through experiments, and demonstrated that airtight structures full of liquid had good resistance to jet penetration. By studying flash radiographs and Autodyn computations, Andersson et al. (1998) concluded that the latter portion of the jet was missing suggesting a large influence of an imploding penetration channel in the process of jet penetration into the targets containing water. From an engineering viewpoint, Li et al. (2002) proposed a new type of protective armor composed of water-filled sealed steel box unit structure, and calculated the interference of this protective armor on SCJ. Gao et al. (2016a & 2016b), Zhang et al. (2017a & 2017b), Guo et al. (2018 & 2019) and Cai et al. (2021) analyzed the process of jet interference by liquid radial reflux when penetrating single-cell liquid-filled composite structure, established and improved the theoretical calculation model of jet disturbed velocity

range, and calculated the residual penetration capacity of SCJ. Tan et al. (2019) and Zu et al. (2019) obtained the relationship between the residual penetration of the jet and the physical parameters of the target, jet, and liquid material through dimensional analysis. Zu et al. (2021) presented experimental and theoretical investigations of the penetration ability of the residual SCJ emerging from the liquid-filled compartment structure after the penetration process at different impact angles.

Although the mechanism of the interaction of an LCA with a SCJ in the case of vertically central penetration has been studied, to the best of our knowledge, the mechanism of interaction between strongly-constrained liquid-filled composite armor (SLCA) and SCJ during eccentric penetration has not been reported in the open literature. The penetration position of jet is random, and the preliminary test results show that the penetration position has a great influence on the anti-penetration performance of SLCA. Therefore, studying the influence of SLCA on the stability of incoming SCJ during eccentric penetration is necessary. In this study, the process of jet eccentricity penetrating SLCA is analyzed by combining theory and experiment. The main contents include three aspects: the crater growing process in the liquid layer of SLCA during the jet’s eccentric penetration, the influence of the eccentric distance on the jet’s interference velocity range, and the influence of the eccentric distance on the lateral movement of the jet element under the impact by shock wave and liquid radial reflux.

## 2 X-RAY EXPERIMENTAL WORK

X-ray experiments were conducted on the process of the SCJ penetrating the SLCA at different eccentricity distances, to display the morphology of the residual jet directly after the interference by the SLCA.

### 2.1 Shaped charge (SC)

Figure 2 shows a picture of a  $\Phi 56$  mm SC. In the experiments, the  $\Phi 56$  mm SC has a charge capacity of 203 g, and the charge type is JH-2 explosive. The jet tip velocity is 6700 m/s and the jet tail velocity is 1200 m/s. At 30  $\mu$ s, the radius of the tip of jet is 1 mm and the tail is 7 mm. The stand-off is 80 mm.

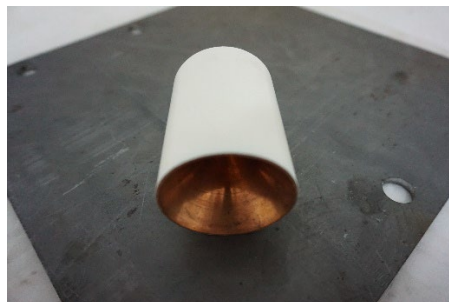


Figure 2 A  $\Phi 56$  mm shaped charge

### 2.2 Strongly-constrained liquid-filled composite armor

The dimensional parameters of the SLCA used in the experiments are shown in Figure 3, and the physical object is shown in Figure 4. As shown, the SLCA consists of a thick metal shell with a cylindrical cavity and threaded holes, a liquid filling material, a cover plate and a seal connected by screws. The outer diameter of the metal shell is 50 mm, the thickness of the side wall is 35 mm, the thickness of the cover plate is 4 mm, the thickness of the bottom of the shell is 10 mm, the metal material is #45 steel, while the radius of the cylindrical cavity is 15 mm, the height is 70 mm, and the filling material is water. The specific material parameters are shown in Table 1.

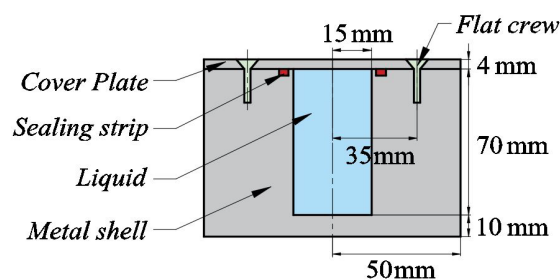


Figure 3 Dimension parameter diagram of SLCA

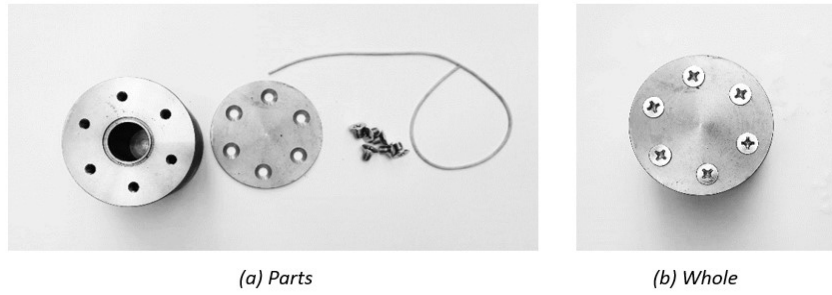


Figure 4 Physical shot of SLCA

Table 1 Material parameters of armor

Materials	$\rho/(\text{kg}\cdot\text{m}^{-3})$	$c/(\text{m}\cdot\text{s}^{-1})$	$\sigma_s/\text{MPa}$	$\sigma_b/\text{MPa}$	$e/\%$
#45 steel	7850	5200	370	630	17
water	1000	1460	—	—	—

### 2.3 Experiment setup

To study the influence of different eccentricity distances on the interfered velocity range of jet and the lateral movement of SCJ element when jet penetrates into SLCA, X-ray experiments are conducted for four working conditions with eccentricity distance of 0, 3, 6, and 9 mm. The included angle between the two light outlets of the X-ray machine is  $45^\circ$ . To facilitate the calculation of the lateral displacement of the SCJ after interference, we ensure that the light direction of light outlets B is perpendicular to the eccentric direction in working conditions 2 and 3.

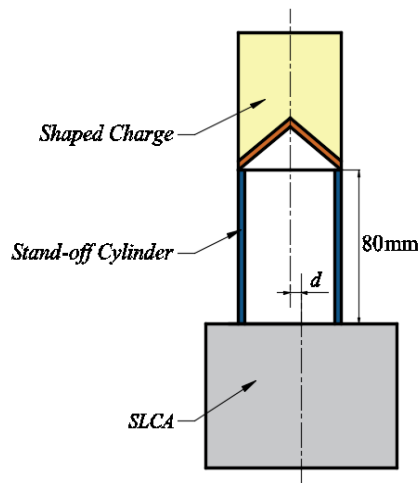


Figure 5 Experiment layout

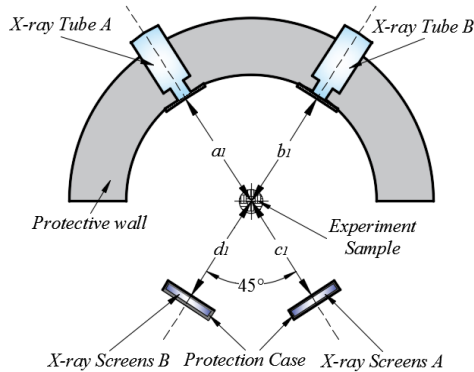


Figure 6 Schematic of X-ray experiment layout



Figure 7 X-ray experiment setup

The X-ray test was set according to Figures 5-7. The distance between the bottom surface of the SLCA and the ground was denoted as  $H_D$ , and the amplification ratio of A and B light outlets was  $k_A = \frac{a_1 + c_1}{a_1}$  and  $k_B = \frac{b_1 + d_1}{b_1}$ , respectively. The X-ray machine output time was set to 70  $\mu\text{s}$  and 90  $\mu\text{s}$ , respectively. Test setting parameters are shown in Table 2.

Table 2 X-ray experimental setting parameters

No.	$d$ (mm)	$H_D$ (m)	$a_1$ (mm)	$b_1$ (mm)	$c_1$ (mm)	$d_1$ (mm)	$k_A$	$k_B$	$T_{AS}$ ( $\mu\text{s}$ )	$T_{BS}$ ( $\mu\text{s}$ )
1	0	1.390	1.435	1.455	2.525	2.625	1.760	1.804	70	90
2	3	1.400	1.385	1.430	2.300	2.340	1.661	1.636	70	90
3	6	1.380	1.360	1.385	2.350	2.440	1.728	1.762	70	90
4	9	1.390	1.405	1.430	2.355	2.530	1.676	1.769	70	90

## 2.4 Experimental results

Figure 8 (a-d) shows the X-ray experiment results. X-ray images at 70  $\mu\text{s}$  showed that when the SCJ penetrates the SLCA, the tip and middle section of the SCJ is severely disrupted, the former section of the SCJ shows a very obvious fracture and fragmentation, the middle starts to exhibit necking and fracture, and the latter section of the jet keeps good collimation and continuity.

In the experiments with eccentric distances of 3, 6, and 9 mm, the tip of jet has obvious lateral movement. Due to the large velocity gradient of the jet, its elements with necking and fracture continue to stretch over time, and the distance between the fractured jet elements also increases. X-ray images at 90  $\mu\text{s}$  show that the jet fracture and lateral movement are further enhanced, and the latter section of jet still maintains good continuity and collimation. In general, the SCJ is disturbed after it penetrates through the SLCA, and the disturbed part of the jet exhibits obvious partition. According to the severity of the interference, the residual SCJ is divided into three parts: serious disturbed, general disturbed, and undisturbed. Among them, the jet elements have obvious lateral displacement, fragmentation and discontinuous distribution in the seriously disturbed part, while the jet has a necking fracture and a small lateral displacement in the general disturbed part. In the undisturbed part, the jet keeps good collimation and continuity.

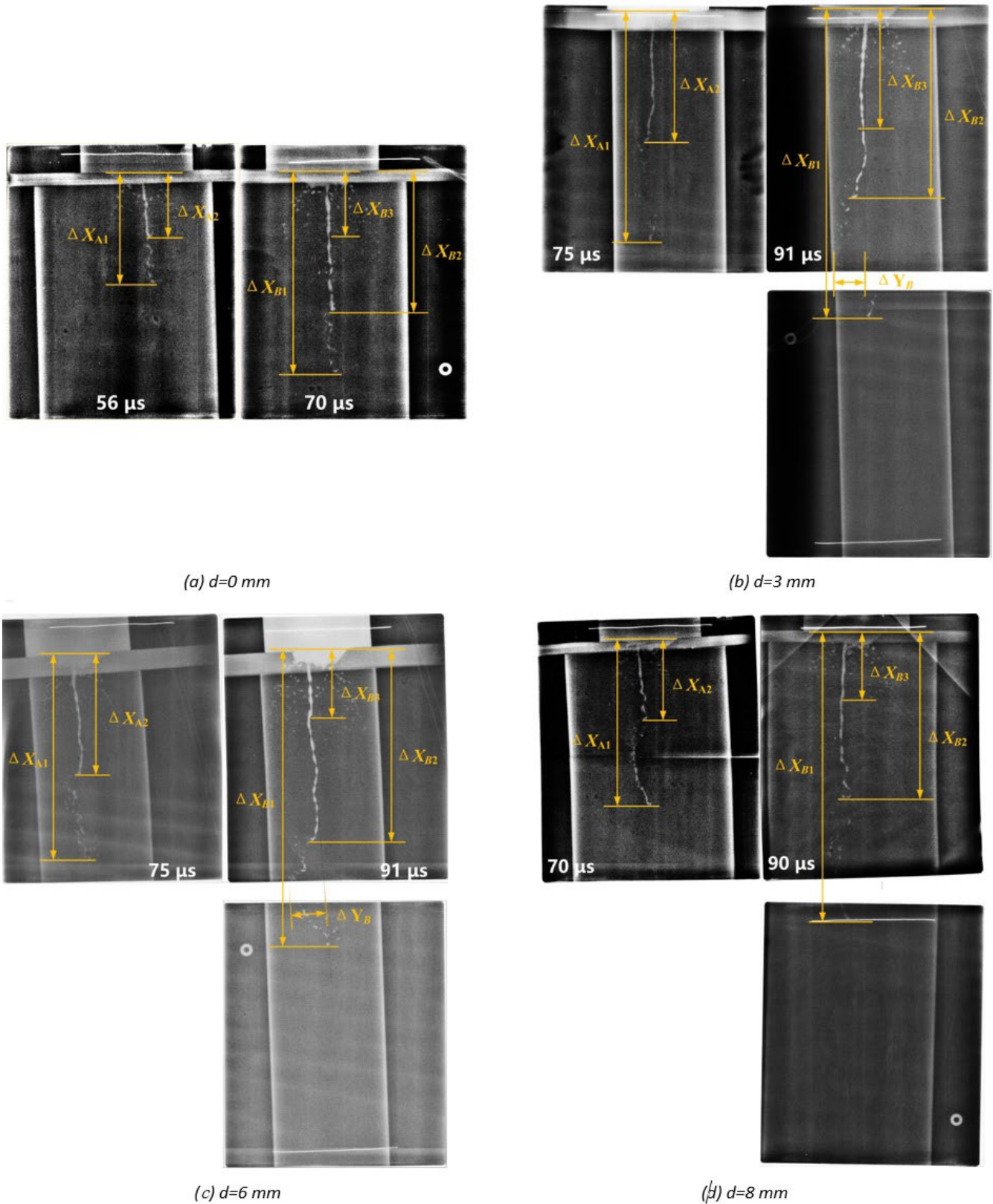


Figure 8 X-ray experiment results

According to the X-ray images at  $T_A$  and  $T_B$ , the velocity at different positions of the jet can be calculated. The following takes working condition 2 as an example to calculate the disturbed velocity range of the jet and the maximum lateral movement of the tip of the jet.

In the axial direction of the SCJ, we take the bottom of the SLCA as the reference. The distance between the tip of jet and the reference line at  $T_A$  and  $T_B$  was denoted as  $\Delta X_{A1}$  and  $\Delta X_{B1}$ . The distance between the boundary point of the serious disturbed part and the general disturbed part of residual jet and the reference line at  $T_A$  and  $T_B$  was denoted as  $\Delta X_{A2}$  and  $\Delta X_{B2}$ . The distance between the boundary point of the general disturbed part and the undisturbed part of residual jet and the reference line at  $T_B$  was denoted as  $\Delta X_{B3}$ . The measured distance and actual output time under each working condition are shown in Table 3.

**Table 3** Experiment data

No.	$d$ (mm)	$T_A$ ( $\mu$ s)	$T_B$ ( $\mu$ s)	$\Delta X_{A1}$ (mm)	$\Delta X_{A2}$ (mm)	$\Delta X_{B1}$ (mm)	$\Delta X_{B2}$ (mm)	$\Delta X_{B3}$ 0(mm)
1	0	56	70	172.5	102.0	311.1	216.6	146.6
2	3	75.7	91	364.0	206.0	495.0	305.0	135.0
3	6	75.5	91	326.6	184.0	474.0	296.0	118.0
4	9	70	90	265.0	126.3	460.5	267.5	86.1

In addition, the velocity gradient of the jet is assumed to be linear. Accordingly, the velocity of the tip of the residual jet  $V_{jr1}$ , the minimum velocity of the serious disturbed part  $V_{jr2}$ , and the minimum velocity of the general disturbed part  $V_{jr3}$  can be calculated as follows:

$$V_{jr1} = \frac{\Delta X_{B1}/k_B - \Delta X_{A1}/k_A}{T_B - T_A}, \tag{1}$$

$$V_{jr2} = \frac{\Delta X_{B2}/k_B - \Delta X_{A2}/k_A}{T_B - T_A}, \tag{2}$$

$$V_{jr3} = V_{jr2} - \frac{\Delta X_{B2} - \Delta X_{B3}}{\Delta X_{B1} - \Delta X_{B2}}(V_{jr1} - V_{jr2}). \tag{3}$$

In the radial direction of the SCJ, taking the central axis of the undisturbed part of the residual jet as the reference, the distance from the maximum lateral displacement point of the residual jet to the reference line at  $T_B$  is denoted as  $\Delta Y_B$ , and the maximum lateral displacement  $s_l$  and lateral movement velocity of the jet  $V_l$  can be calculated as follows:

$$s_l = \frac{\Delta Y_B}{k_B}, \tag{4}$$

$$V_l = \frac{\Delta Y_B/k_B}{t_l}. \tag{5}$$

Similarly, the velocity range of disturbed jet, the maximum lateral displacement of disturbed jet, and the jet particle velocity at the maximum lateral displacement at different eccentric distances can be calculated. The results are shown in Table 4.

**Table 4** Experiment parameters and result statistics

No.	$d$ (mm)	Serious disturbed part (m/s)	General disturbed part (m/s)	Velocity of jet element with maximum lateral displacement (m/s)	Maximum lateral displacement (mm)
1	0	[4438,5319]	[3097,4438]	—	—
2	3	[4035,5393]	[2819,4035]	4814	29.120
3	6	[3972,5167]	[2755,3972]	4481	27.191
4	9	[3802,5110]	[2477,3802]	4394	—

### 3 THEORETICAL ANALYSIS

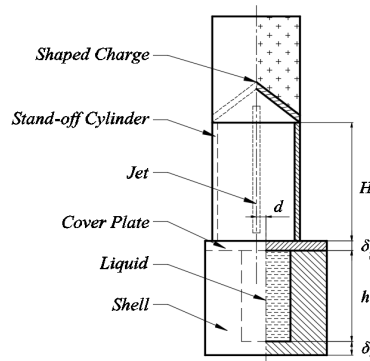


**Figure 9** Schematic of eccentric penetration process

Figure 9 shows the schematic of SCJ eccentrically penetrating into SLCA. When this occurs, the stability of the SCJ is affected by the shock wave and asymmetric liquid reflux impact, resulting in an obvious lateral movement, which reduces the subsequent penetration capacity of the residual jet. In this paper, the interaction between SCJ and SLCA during eccentric penetration is analyzed theoretically from three aspects: the crater growing process of SCJ in liquid layer, the interference process of shock wave propagation and liquid radial reflux on jet, and the lateral movement process of jet elements by lateral force.

#### 3.1 Crater growing process of SCJ in liquid layer of SLCA during eccentric penetration

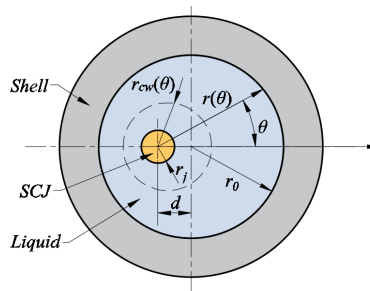


**Figure 10** Crater growing process of jet in liquid layer

Figure 10 shows the crater growing process in the liquid layer when the SCJ eccentrically penetrates the SLCA. The liquid cross section is taken at a certain height  $h_w$ , and the polar coordinate system is established with the central point of the jet's penetration position. Then, the relationship between the position of the inner cavity wall  $r(\theta)$  and the eccentricity distance  $d$  can be expressed as

$$(r(\theta) \cos \theta - d)^2 + (r(\theta) \sin \theta)^2 = r_0^2, \tag{6}$$

When the eccentricity distance  $d$  is greater than zero, the distance from the coordinate origin to the inner cavity wall  $r(\theta)$  varies everywhere within the range of  $[0, 180^\circ]$ , and corresponding parameters such as subsequent penetration

crater size, liquid internal pressure, reflection time of shock wave, liquid reflux speed, and interference time are also different with the change of angle.

Considering the influence of shock wave and compressibility of liquid on the growth process of jet penetration crater, this study makes the following assumptions:

1. The radial and axial pressures of the initial reaming are equal.
2. The radial reaming pressure decreases with the increase of the crater size, and the product of radial reaming pressure and penetration crater area is constant.
3. The circumferential motion of liquid particles is ignored, and the mutual interference of liquid particles in the circumferential direction is ignored.
4. In a constrained structure, the strength of the liquid is considered equal to the internal pressure of the liquid because the liquid is compressed.

According to assumption 1, when the jet penetrates the liquid layer at a certain height  $h_w$ , the jet penetration pressure  $p_j$  can be calculated as follows:

$$p_j = \frac{1}{2} \rho_j (v_j - w)^2. \tag{7}$$

According to Bernoulli equation, in the process of crater size growth, the stagnation pressure at the crater wall is equal to the sum of dynamic pressure and static pressure at the crater wall. Then, the stagnation pressure can be calculated:

$$p(\theta) = \frac{1}{2} \rho_w(\theta) u_c^2(\theta) + R_w(\theta). \tag{8}$$

According to assumption 2, there is

$$p(\theta) = p_j \cdot \frac{r_j^2}{r_c^2(\theta)}. \tag{9}$$

The liquid is compressed in the process of reaming. Based on the research of Dowson and Higginson (2014), the relationship between liquid pressure and density is

$$p_w(\theta) = \frac{\rho_w(\theta)/\rho_{w0} - 1}{2.3 \times 10^{-9} - 1.7 \times 10^{-9} \rho_w(\theta)/\rho_{w0}}. \tag{10}$$

According to assumption 3, the liquid density can be approximated as

$$\rho_w(\theta) = \frac{r^2(\theta)}{r^2(\theta) - r_c^2(\theta)} \rho_{w0}. \tag{11}$$

According to assumption 4, there is

$$R_w(\theta) = p_w(\theta). \tag{12}$$

Substituting equation (9–12) into equation 8, there is

$$\frac{1}{2} \rho_j (v_j - u)^2 \cdot \frac{r_j^2}{r_c^2(\theta)} = \frac{1}{2} \rho_{w0}(\theta) u_c^2(\theta) + \frac{r_c^2(\theta)}{0.6 \times 10^{-9} r^2(\theta) - 2.3 \times 10^{-9} r_c^2(\theta)} \tag{13}$$

Then, the remaining velocity of the SCJ in the liquid layer of the SLCA is

$$u_c(\theta) = \sqrt{\frac{\rho_j}{\rho_{w0}} \cdot \frac{r_j^2}{r_c^2(\theta)} (v_j - u)^2 - \frac{2}{\rho_{w0}} \cdot \frac{r_c^2(\theta)}{0.6 \times 10^{-9} r^2(\theta) - 2.3 \times 10^{-9} r_c^2(\theta)}} \tag{14}$$

The remaining velocity  $u_c(\theta)$  decreases with the increase of penetration crater size. When remaining velocity  $u_c(\theta)$  decreases to zero, the penetration crater of jet reaches the maximum value remaining velocity  $r_{cw}(\theta)$ .

When the jet remaining occurs in the liquid, the actual crater size becomes slightly larger than the calculated maximum crater size  $r_{cw}(\theta)$  until negative pressure is generated in the cavity. When the pressure of the compressed part of the liquid exceeds the equilibrium pressure, the liquid undergoes self-reflux under the action of pressure difference to shrink the crater. However, due to the extremely fast propagation speed of shock wave, in this process, it is considered that the self-reflux of liquid under the action of differential pressure and the expansion exceeding the equilibrium pressure cancel each other. Therefore, we assume that the equilibrium state is maintained after the penetration crater of the remaining reaches the calculated maximum crater size  $r_{cw}(\theta)$  until the reflected shock wave propagates to the crater wall. In addition, since the jet tail diameter is approximately 6 mm, this study only analyzes the eccentricity distance within the interval [0 mm, 12 mm] without considering the direct interference between the jet and the inner cavity wall of SLCA.

Matlab was used to calculate the remaining process at  $h_w = 0$ , and the relationship between the maximum penetration crater size  $r_{cw}(\theta)$  and angle  $\theta$  at [0, 180°] with different eccentricity distances  $d$  at [0 mm, 12 mm] was drawn as shown in Figure 11. Figure 12 shows the relationship between the remaining size  $r_c(\theta)$  and time  $t$  at angle  $\theta = 0$  and  $\theta = \pi$  under different eccentricity distances, while Figure 13 shows the relationship between the remaining velocity  $u_c(\theta)$  and time  $t$  at angle  $\theta = 0$  and  $\theta = \pi$  under different eccentricity distances. As shown in Figure (11–13), with the increase of eccentric distance, the difference of crater size between different angles gradually increases, and the difference of crater size change and remaining velocity change at  $\theta = 0$  and  $\theta = \pi$  also becomes increasingly obvious.

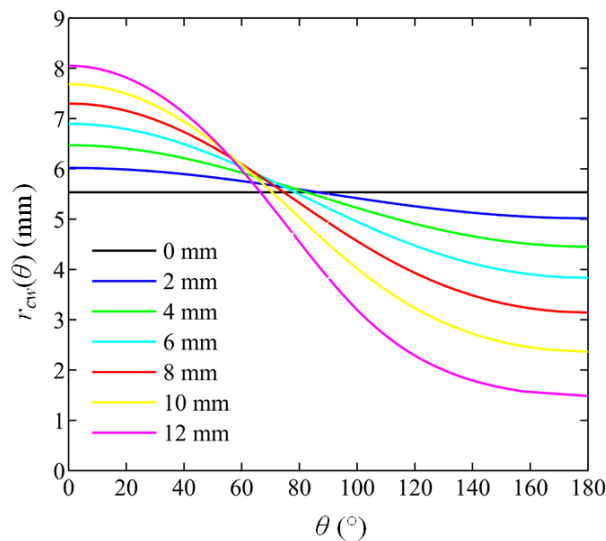


Figure 11 Relationship between maximum penetration crater size and angle

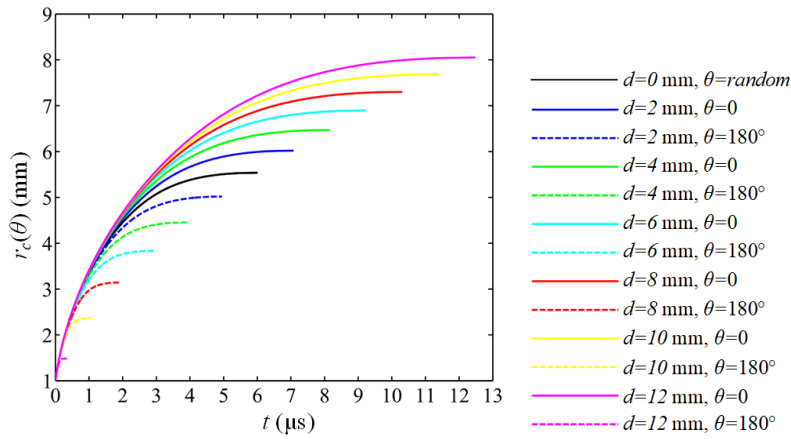


Figure 12 Relationship between reaming size and time

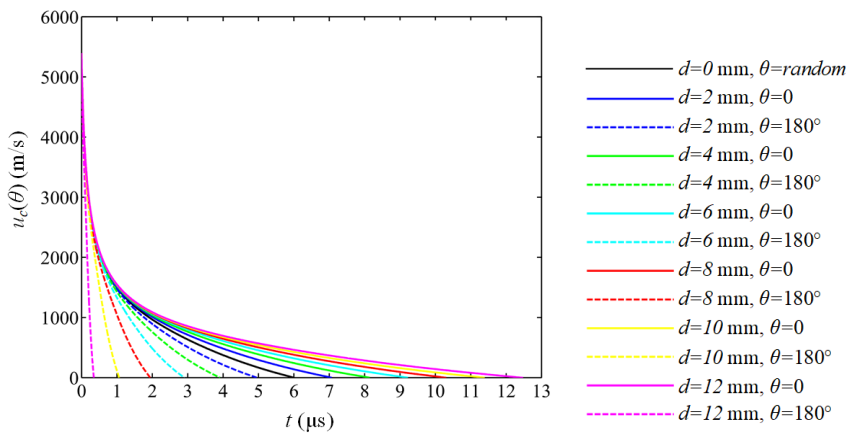


Figure 13 Relationship between reaming velocity and time

Figure 14 shows the ratio of the maximum and minimum pressure of the liquid at  $h_w = 0$  when the jet reaming reaches the maximum crater size at different eccentric distances.

When the eccentric distance  $d$  increases to 12 mm, the maximum pressure ratio between  $p_w(\pi)$  and  $p_w(0)$  is 3.37, within an order of magnitude. Therefore, it is feasible to ignore the circumferential motion of the liquid particles in the process of jet reaming and liquid radial reflux for the convenience of calculation.

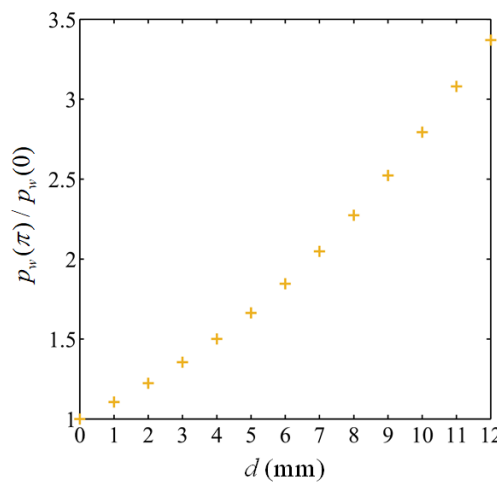


Figure 14. Ratio of maximum to minimum pressure  $p_w(\pi)/p_w(0)$  in liquid cross section

### 3.2 Shock wave propagation and liquid radial reflux during eccentric penetration

#### 3.2.1 Calculation of effective interference angle range

When the SCJ centrally penetrates into the SLCA, the liquid particles at the crater wall of the same liquid level converge to the center and act on the jet surface simultaneously driven by the reflected shock wave.

As shown in Figure 15, in the case of eccentric penetration, due to the circular shape of the inner cavity of the SLCA, there is an effective reflection angle for shock wave reflection on the inner cavity wall, and only the reflected shock wave generated within the effective interference angle can drive the liquid particles at the crater wall to contact with the jet surface. Meanwhile, at the same liquid level, the time of shock wave propagating along different angles and the time of liquid particles converging and returning to the jet surface driven by reflected shock wave are different. The effective interference angle interval of the SLCA interference the SCJ in eccentric penetration is calculated.

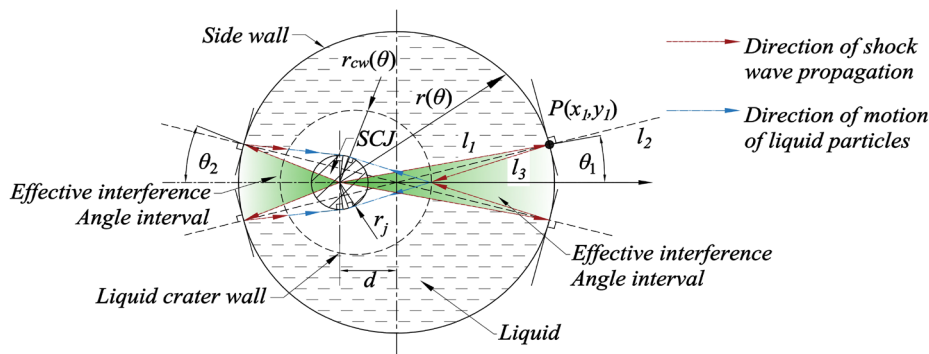


Figure 15 Schematic of effective interference angle range during eccentric penetration

The section with the height of liquid level  $h_w$  was taken for analysis, and a limit interference angle was observed on both sides of the jet penetration position so that the liquid particles driven by the reflection shock wave could collide with the jet.

The limit interference angle in the first and second quadrants are denoted as  $\theta_1$  and  $\theta_2$ , and  $P(x_1, y_1)$  is the reflection point of the shock wave at the limit interference angle on the cavity wall. The effective angle range of jet disturbed can be calculated by using the following geometric relations:

$$k_1 = y_1/x_1, \tag{15}$$

$$k_2 = y_1/(x_1 - d), \tag{16}$$

$$(x_1 - d)^2 + y_1^2 = r_0^2, \tag{17}$$

$$(k_2 - k_1)/(1 + k_1k_2) - (k_3 - k_2)/(1 + k_2k_3) = 0, \tag{18}$$

$$|y_1 - k_3 \cdot x_1|/\sqrt{(k_3^2 + 1)} = r_j. \tag{19}$$

where  $k_1$  is the slope of incoming ray  $l_1$ ,  $k_2$  is the slope of symmetric line  $l_2$ , and  $k_3$  is the slope of reflected ray  $l_3$ .

The positions of limit reflection points at different eccentric distances can be obtained by simultaneous equations. When  $P(x_1, y_1)$  is in the first quadrant, there is  $\theta_1 = \arctan(y_1/x_1)$ , and when  $P(x_1, y_1)$  is in the second

quadrant, there is  $\theta_2 = -\arctan(y_1/x_1)$ . Then, the effective interference angle interval can be expressed as  $\theta \in [-\theta_1, \theta_1] \cup [180^\circ - \theta_2, 180^\circ + \theta_2]$ .

Matlab is used to draw the variation trend of  $\theta_1$  and  $\theta_2$  with eccentric distance  $d$  and the effective interference angle interval with the eccentric distance, as shown in Figures 16 and 17.

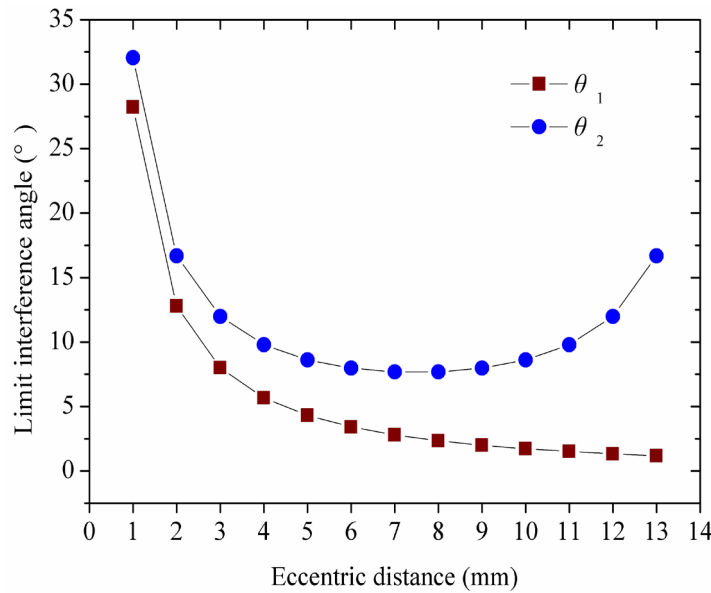


Figure 16 Variation trend of limit interference angle with eccentric distance

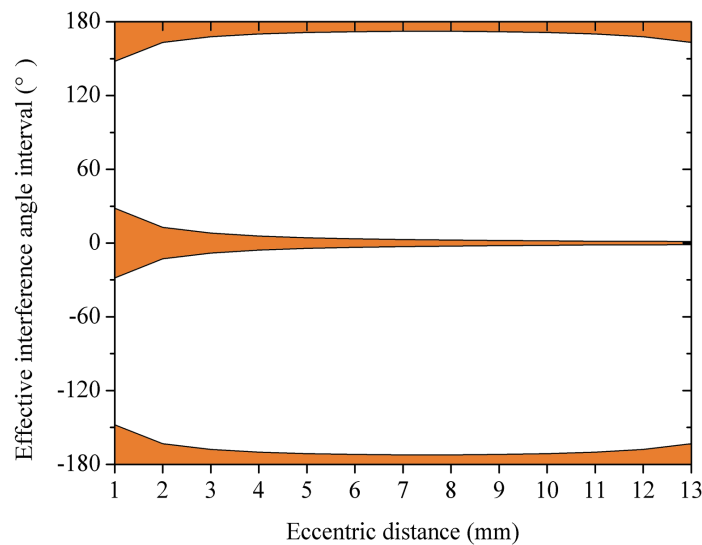


Figure 17 Variation trend of effective interference angle interval with eccentric distance

### 3.2.2 Calculation of interference velocity range of jet

The following discussion and calculation of the interference velocity range of jet are carried out within the angle range of effective reflection interference, that is,  $\theta \in [-\theta_1, \theta_1] \cup [180^\circ - \theta_2, 180^\circ + \theta_2]$ .

#### (a) Calculation of side-wall reflection reflux interference velocity interval

The jet penetrates into the liquid layer and generates an initial shock wave, which propagates to the side-wall of the cavity and is reflected. Then, the reflected shock wave propagates to the liquid crater wall and is reflected on the free surface, driving the liquid particles to reflux radially to the jet surface and interfering with the stability of the jet, as shown in Figure 18.

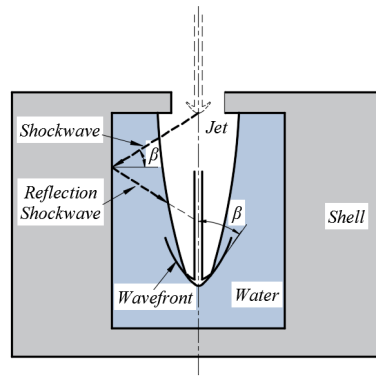


Figure 18 Schematic of shock wave propagation and reflection

Based on the assumption that the action time of the disturbance pulse generated by the initial shock wave is the time difference between the propagation of the shock wave along the direction of Mach angle and the radial direction, the maximum and minimum interference velocity of jet affected by the initial shock wave generated when jet penetrates to the depth  $h_w$  of liquid layer can be calculated as

$$v_{jd1}(\theta) = \frac{z_0 + H + \delta_f + h_w + (2r(\theta) - r_j - r_{cw}(\theta)) \tan \beta}{t_{jw} + t_{s1}(\theta) + t_{cs1}(\theta)}, \tag{20}$$

$$v_{jd2}(\theta) = \frac{z_0 + H + \delta_f + h_w}{t_{jw} + t_{s2}(\theta) + t_{cs2}(\theta)}, \tag{21}$$

where,  $z_0$  is the position of virtual origin,  $H$  is stand-off,  $\delta_f$  is the thickness of cover plate,  $\beta$  is Mach angle,  $t_{jw}$  is the corresponding moment when the jet penetrates to depth  $h_w$  in the liquid layer,  $t_{s1}(\theta)$  and  $t_{s2}(\theta)$  are the propagation time of shock wave propagating to the liquid crater wall along two different paths, and  $t_{cs1}(\theta)$  and  $t_{cs2}(\theta)$  are the time consumed by liquid particles at the crater wall to return to the jet surface driven by shock wave.

Therefore, on the side-wall reflection reflux interference stage, the velocity range of jet interfered by liquid particles is  $[v_{jd2}(\theta)|_{h_w=h}, v_{jd1}(\theta)|_{h_w=0}]$ . The relationship between jet velocity range interfered by the side-wall reflection reflux and eccentric distance is shown in Figure 19.

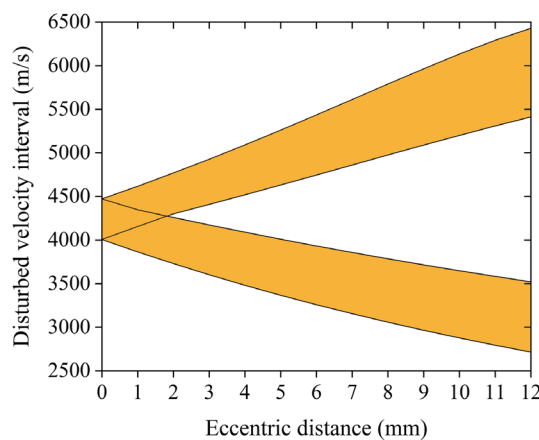


Figure 19 Variation of side-wall interference velocity interval with eccentric distance

(b) Calculation of maximum jet velocity interfered by bottom reflection reflux

When the SCJ penetrates the bottom plate of SLCA, the shock wave is reflected on the interface between the liquid and bottom plate. The bottom reflected shock wave propagates to the liquid crater wall and causes secondary reflection at the free interface, which makes the liquid particles reflux radially. The maximum velocity of the interference jet affected by bottom reflection reflux can be calculated as follows:

$$v_{jd3}(\theta) = \frac{z_0 + H + \delta_f + h}{t_{jw}|_{h_w=h} + t_{s3}(\theta) + t_{cb}(\theta)}, \tag{22}$$

where,  $t_{s3}(\theta)$  is the time for the bottom reflected shock wave to propagate to the crater wall, and  $t_{cb}(\theta)$  is the time consumed by liquid particles at the bottom crater wall to reflux to the jet surface.

(c) Calculation of direct interference region by side-wall reflected shock wave

When the SCJ penetrates the bottom plate of SLCA, the liquid is sprayed from the crater and contacts with the jet due to the large pressure difference at the internal and external of the SLCA. In the bottom region, the side-wall reflected shock wave acts directly on the jet surface with the liquid as the carrier. The maximum and minimum velocity of the disturbed jet in this region can be calculated as follows:

$$v_{jd4}(\theta) = \frac{z_0 + H + \delta_f + h}{t_{jw}|_{h_w=h-2(r(\theta)-r_j)\tan\beta} + t_{s4}(\theta)}, \tag{23}$$

$$v_{jd5}(\theta) = \frac{z_0 + H + \delta_f + h}{t_{jw}|_{h_w=h} + t_{s5}(\theta)}, \tag{24}$$

where,  $t_{s4}(\theta)$  and  $t_{s5}(\theta)$  are the propagation time of shock wave to the liquid crater wall along two different paths.

Therefore, the velocity range of direct interference by side-wall reflected shock wave is  $[v_{jd5}(\theta), v_{jd4}(\theta)]$ , and the relationship between the interference velocity range and the eccentric distance is shown in Figure 20. Due to the large pressure on the jet in the direct interference region by side-wall reflected shock wave and the bottom reflected interference region, the jet particles are considered to be seriously disturbed. Therefore, the serious disturbed part of jet is  $[v_{jd5}(\theta), v_{jd3}(\theta)]$ .

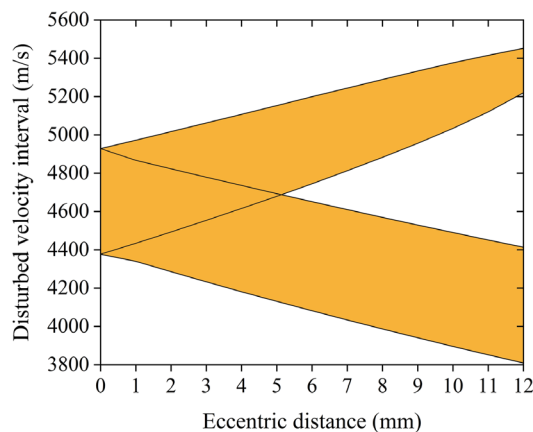


Figure 20 Variation of velocity interval of direct interference with eccentric distance

(d) Calculation of interference velocity interval by bottom secondary reflection shock wave

The bottom reflected shock wave propagates to the side-wall of the cavity and is reflected to form a secondary reflected shock wave. The secondary reflected shock wave propagates to the liquid crater wall and drives the liquid particles to reflux and interference with the jet again.

The simulation by Cai et al. (2021) showed that the bottom secondary reflected shock wave interacts with the side-wall reflected shock wave during propagation, thereby weakening the wave front pressure to a certain extent. Moreover, after the liquid particles complete the first radial reflux, the jet impacts on the liquid particles to make the second reaming. However, due to the decrease of the jet impact pressure and the existence of liquid motion inertia, the cavity size of the liquid secondary reaming is small, which is ignored in the calculation. The maximum and minimum velocity disturbed jet by the secondary reflection shock wave can be calculated as follows:

$$v_{jd6}(\theta) = \frac{z_0 + H + \delta_f + h - 2(r(\theta) - r_j)\tan\beta}{t_{jw}|_{h_w=h} + t_{rs1}(\theta)}, \tag{25}$$

$$v_{jd7}(\theta) = \frac{z_0 + H + \delta_f + h}{t_{jw}|_{h_w=h} + t_{rs2}(\theta)}, \tag{26}$$

Therefore, the interference velocity range of the bottom secondary reflection is  $[v_{jd7}(\theta), v_{jd6}(\theta)]$ , and the relationship between the interference velocity range and the eccentric distance is shown in Figure 21.

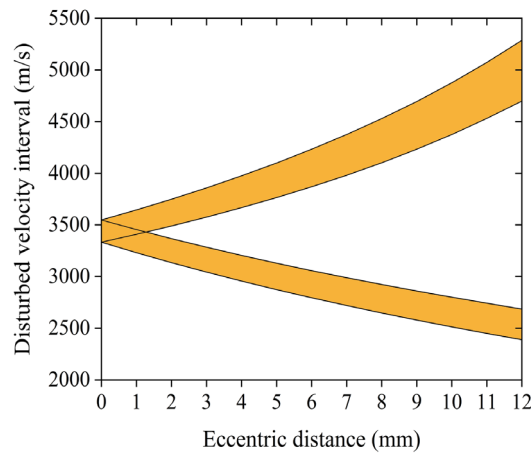


Figure 21 Variation of interference velocity range with eccentric distance

To sum up, the total velocity range of the disturbed jet is  $[v_{jd7}(\theta), v_{jd5}(\theta)]$ , in which the serious disturbed part is  $[v_{jd4}(\theta), v_{jd5}(\theta)]$  and the general disturbed part is  $[v_{jd7}(\theta), v_{jd4}(\theta)]$ .

### 3.3 Calculation of maximum lateral displacement of jet during eccentric penetration

When the jet penetrates into the SLCA along the central axis of symmetry, the force of liquid reflux on the jet surface is equal in all directions, and the jet is clipped. Due to the shaped charge processing technology, material uniformity and other factors, the fracture jet has a small lateral motion velocity. When the jet eccentrically penetrates the SLCA, an obvious lateral movement occurs due to the different forces in each direction of the jet element. Section 2.2 shows some overlap in the velocity range of the disturbed jet, and it is difficult to calculate the lateral displacement of the overlapped part. Therefore, the lateral movement of the jet element under unilateral force is solved here.

The action time of shock wave on the jet element is  $\Delta t_l = 4r_j/c_j$ . If the acting time difference of the direct interference of the side-wall reflection shock wave on the both sides of the penetration position is greater than  $\Delta t_l$ , that is,  $t_{s5}(\theta) - t_{s4}(\theta) > \Delta t_l$ , a direct interference region exists, affected by only the unilateral lateral force by the side-wall reflection shock wave, and the maximum velocity of this disturbed region is  $v_{jd4}(\theta)$ . In the region affected by unilateral transverse force, the shock wave directly acts on the SCJ and reflects on the jet surface, resulting in lateral displacement of the jet elements. The maximum lateral displacement of jet can be obtained according to force analysis as shown in Figure 22.

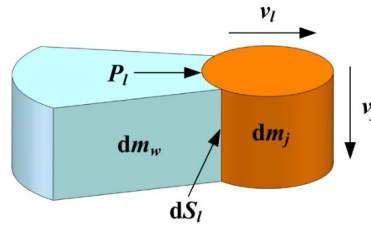


Figure 22 Schematic of force analysis of jet element

The change of the axial velocity of the jet and the effect of sparse waves on the interaction between liquid and jet elements are ignored. Regardless of the wave front pressure and particle velocity, the relationship between the lateral velocity of the jet element  $v_l$  and the lateral force  $P_l$  by shock wave can be obtained as equation 27, according to the momentum conservation theorem.

$$\frac{dm_j}{dS_l} \cdot \frac{dv_l}{dt} = P_l, \tag{27}$$

$$P_l = KP_{jw} e^{t_{sl}/\tau}, \tag{28}$$

where  $dm_j$  is the mass of the jet element,  $dS_l$  is the contact area between the liquid and jet,  $K$  is the reflection coefficient of shock wave,  $\tau$  is the time constant,  $t_{sl}$  is the propagation time of shock wave. The maximum lateral displacement can be calculated as follows:

$$s_l = v_l \cdot t_l, \tag{29}$$

where  $t_l$  is the time difference between the time of X-ray emission and the time of side-wall reflection shock wave reflected on the jet surface.

## 4 COMPARISON BETWEEN EXPERIMENTAL RESULTS AND THEORETICAL RESULTS

### 4.1 Interference velocity interval

When the jet penetrates into the SLCA, lateral movement and fracture occur due to shock wave and liquid reflux impact. With the change of eccentricity distance, the velocity range of the disturbed jet is also changed. Table 5 presents statistics of theoretical calculation results and experimental results of jet disturbed velocity interval at different eccentricity distances (0, 3, 6, and 9 mm). With the change of eccentricity distance, the theoretical calculation results of the jet disturbed velocity interval are in good agreement with the experimental results. When the eccentricity distance is 0, 3, 6, and 9 mm, the minimum velocity in the severely disturbed part calculated by theory is 4377, 4233, 4082, and 3941 m/s, respectively, and the errors are 1.39%, 4.61%, 2.69%, and 3.53%, respectively. The minimum velocities in the general interference part calculated by theory are 3333, 3044, 2795, and 2579 m/s, and the errors are 7.08%, 7.39%, 1.43%, and 3.96%, respectively.

Table 5 Comparison between theoretical and experimental results of disturbed velocity interval

No.	$d$ (mm)	Serious disturbed part (m/s)		General disturbed part (m/s)	
		Theory	Experiment	Theory	Experiment
1	0	[4377, 5243]	[4438, 5319]	[3333, 4377]	[3097, 4438]
2	3	[4233, 5243]	[4035, 5393]	[3044, 4233]	[2819, 4035]
3	6	[4082, 5243]	[3972, 5167]	[2795, 4082]	[2755, 3972]
4	9	[3941, 5243]	[3802, 5110]	[2579, 3941]	[2477, 3802]

Figure 23 more intuitively shows the distribution of the jet disturbed velocity interval calculated by theoretical calculation and X-ray test with the change of eccentric distance. The jet disturbed velocity interval calculated by theoretical calculation is in good agreement with the X-ray test result, which indicates the accuracy of the theoretical calculation model.

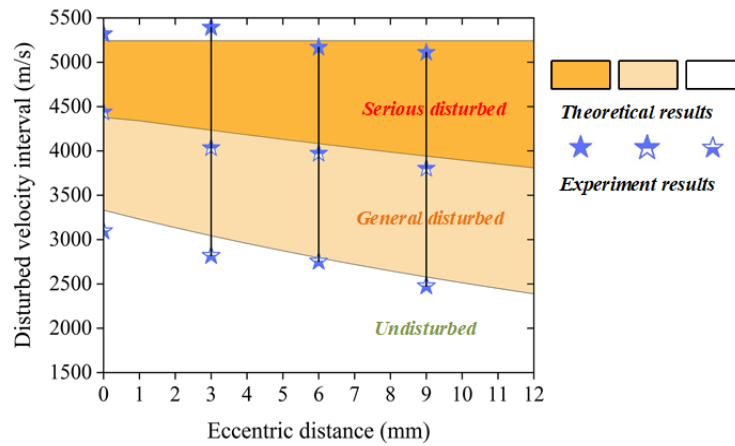


Figure 23 Comparison between theoretical and experimental results of disturbed velocity interval

#### 4.2 Maximum lateral displacement of jet element

As shown in Table 6, the theoretical calculation and experimental results of the maximum velocity and maximum lateral distance of the jet element with the unilateral force at different eccentricity distances (3, 6, and 9 mm) are summarized. The theoretical calculation results are all within the acceptable error range.

Table 6 Comparison between theoretical calculation and experimental results

No.	$d$ (mm)	$T_B$ ( $\mu$ s)	$v_{jd4}(0)$ (m/s)		Errors (%)	$s_l$ (mm)		Errors (%)
			Theory	Experiment		Theory	Experiment	
1	0	70	—	—	—	—	—	—
2	3	91	4779	4814	0.73	27.51	29.120	5.85
3	6	91	4651	4481	3.66	25.93	27.191	4.86
4	9	90	4529	4394	2.98	24.56	—	—

Figure 24 shows the relationship between the velocity of jet element with maximum lateral displacement  $v_{jd4}(0)$  and the eccentric distance  $d$ . With the increase of the eccentric distance, the velocity of the jet element with maximum lateral displacement decreases. Compared with the X-ray experimental results, the velocity of the jet element with maximum lateral displacement calculated by theory is 4779, 4651, and 4529 m/s, respectively, and the errors are 0.73%, 3.66%, and 2.98%, respectively, when the eccentricity distance is 3, 6, and 9 mm.

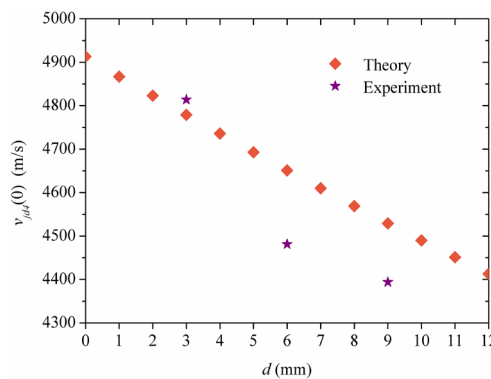


Figure 24 Variation of  $v_{jd4}(0)$  with  $d$ .

The maximum lateral velocity and maximum lateral displacement caused by the interference at different eccentric penetration distances are calculated, as shown in Figures 25 and 26. Compared with the X-ray test results, when the eccentricity distance is 3 mm and 6 mm, the maximum lateral velocity of the jet element calculated by theory is 521.6 m/s and 501.6 m/s, and the errors are 5.45% and 4.76%, respectively. The maximum lateral displacement of the jet element at 91  $\mu$ s is 27.51 mm and 25.93 mm, respectively, and the error is 5.85% and 4.86%, respectively. The errors between the theoretical calculation and experimental results is within the allowable error range, which also proves the accuracy of the theoretical analysis.

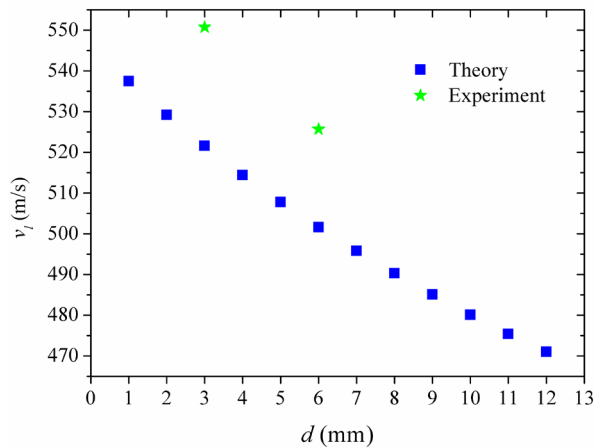


Figure 25 Relationship between maximum lateral velocity and eccentric distance

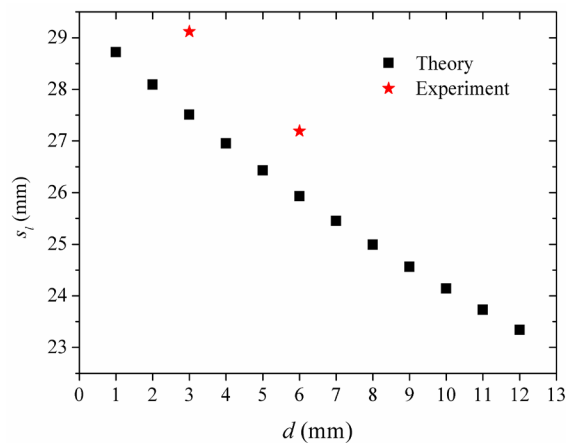


Figure 26 Relationship between maximum lateral displacement and eccentric distance

## 5 CONCLUSIONS

When the jet eccentrically penetrated into the liquid composite armor, it showed obvious lateral displacement due to the shock wave and asymmetric reflux impact of the liquid. On the basis of neglecting the circumferential motion of the liquid, the jet reaming process of eccentric penetration in the liquid layer of the SLCA, the variation of jet disturbed velocity interval in different eccentricity distances, and the relationship between the maximum lateral displacement and the eccentricity distance are analyzed in this paper. The following conclusions are obtained:

- 1) After the SCJ penetrates through the SLCA, sections with different shapes appear due to interference, which can be divided into serious disturbed part, general disturbed part, and undisturbed part according to the severity of interference.
- 2) In the eccentricity distance range [0 mm, 12 mm], the severely disturbed velocity range and total disturbed velocity range of the jet increase with the increase of eccentricity distance.
- 3) Different from the center penetration, in the eccentricity distance interval [1 mm, 12 mm], the tip of the SCJ has a large lateral displacement, which decreases slightly with the increase of the eccentricity distance, and the position of the maximum interference point also moves backward with the increase of the eccentricity distance.

## Acknowledgement

This study is supported by the Jiangsu Province Graduate Research and Practice Innovation Program (grant number KYCX20\_0308) and the National Natural Science Foundation of China (grant number 11602110).

**Author's Contributions:** Writing - original draft, You-er CAI; Test technical support, Xudong ZU, Zhengxiang HUANG, Yaping TAN; Writing - review & editing, Xudong ZU, Xiaojun SHEN, Xin JIA; Supervision, Zhengxiang HUANG.

**Editor:** Marcilio Alves

## References

- Andersson, G.; Karlsson, S.; Watterstam, A. Shaped charge jet interaction with confined water. In Proceedings of the 12th international symposium on ballistics, Hyderabad, India, 3–8 November 1998; pp. 183–190.
- Cai, Y., Zu, X., Tan, Y., & Huang, Z. Study on the Interference Process of Liquid Radial Reflux on the Stability of a Shaped Charge Jet. *Applied Sciences* 2021, 11(17), 8044.
- Dowson D, Higginson GR. (2014). *Elasto-hydrodynamic lubrication (International Series on Materials Science and Technology)*. Elsevier.
- Fourest T, Laurens JM, Deletombe E, Dupas J, Arrigoni M. Confined Rayleigh–Plesset equation for hydrodynamic ram analysis in thin-walled containers under ballistic impacts. *Thin-Walled Structures*, 2015, 86: 67-72.
- Gao, Z.; Huang, Z.; Guo, M.; Zu, X.; Xiao, Q.; Jia, X. Anti-penetration performance analysis of diesel oil filled airtight structures against shaped charge jet. *J. Vib. Shock* 2016a, 35. (In Chinese).
- Gao, Z.Y.; Huang, Z.X.; Guo, M.; Zu, X.D.; Xiao, Q.Q.; Jia, X. Theoretical Study of a Diesel-Filled Airtight Structure Unit Subjected to Shaped Charge Jet Impact. *Propellants Explos. Pyrotech.* 2016b, 41, 62–68.
- Guo, M.; Zu, X.-d.; Huang, Z.-x.; Shen, X.-j. Mechanism of hermetic single-cell structure interfering with shaped charge jet. *Lat. Am. J. Solids Struct.* 2018, 15, <https://doi.org/10.1590/1679-78254977>.
- Guo, M.; Zu, X.D.; Shen, X.J.; Huang, Z.X. Study on liquid-filled structure target with shaped charge verticality penetration. *Def. Technol.* 2019, 15, 861–867.
- Held, M. Verification of the equation for radial crater growth by shaped charge jet penetration. *Int. J. Impact Eng.* 1995, 17, 387-398.
- Held, M.; Backofen, J.E. (1990). Penetration of shaped charge into water. Presented at the 12th International Symposium on Ballistics, San Antonio, TX, USA, 30 October–1 November 1990.
- Held, M.; Huang, N.S.; Jiang, D.; Chang, C.C. Determination of the crater radius as a function of time of a shaped charge jet that penetrates water. *Propellants Explos. Pyrotech.* 1996, 21, 64–69.
- Lee M, Longoria R G, Wilson D E. An extended hydraulic ram model. *ASME-PUBLICATIONS-PVP*, 1996, 325: 75-82.
- Lee M, Longoria R G, Wilson D E. Ballistic waves in high-speed water entry[J]. *Journal of fluids and Structures*, 1997, 11(7): 819-844.
- Lee, E.S.; Oh, K.H.; Song, S.Y. Penetration of particulated shaped charge jet into water. *High-Speed Photography and Photonics: International Congress*. In Proceedings of the International Society for Optics and Photonics, Taejon, Korea, 30 May 1995; pp. 975-981.
- Li, Y.; Gao, F.; Wang, C.; Gao, J. Engineering algorithm for a new type of protective armor disturbing jet penetration. *Acta Armamentarii* 2002, 23, 546–550. (In Chinese)
- Lundstrom E A, Fung W K. *Fluid Dynamic Analysis of Hydraulic Ram IV. (User's Manual for Pressure Wave Generation Model)*. Naval Weapons Center China Lake CA, 1976.
- Lundstrom EA. *Structural response of flat panels to hydraulic ram pressure loading*. Naval Weapons Center China lake CA, 1988.
- Tan, Y.; Jia, X.; Huang, Z.; Cai, Y.; Zu, X. Effect of Liquid Parameters on Protective Performance of a Liquid Composite Target Subjected to Jet Impact. In Proceedings of the 15th Hypervelocity Impact Symposium, Destin, FL, USA, 14–19 April 2019.

Thomas F, Jean-Marc L, Eric D, Jacques D, Michel A. Analysis of bubbles dynamics created by Hydrodynamic Ram in confined geometries using the Rayleigh–Plesset equation. *International Journal of Impact Engineering*, 2014, 73: 66-74.

Truscott T T, Epps B P, Belden J. Water entry of projectiles. *Annual review of fluid mechanics*, 2014, 46: 355-378.

White, J.J.; Wahll, M.J. Shaped charge jet interactions with liquids. In *Proceedings of the 6th International Symposium on Ballistics*, ADPA Orlando, FL, USA, 1981; pp. 554–561.

Zhang, X.; Zu, X.D.; Huang, Z.X.; et al. Interference Characteristics of Liquid Composite Armor of Cell Structure against Jet; *Ordnance Industry Automation*: 2017a. (In Chinese).

Zhang, X.; Zu, X.D.; Huang, Z.X.; Xiao, Q.Q.; Jia, X. Analysis of liquid-filled unit cell structure subjected to shaped charge jet impact. *Explos. Shock Waves* 2017b, 37, 1101–1106. (In Chinese).

Zu, X.; Dai, W.; Huang, Z.; Yin, X. Effects of Liquid Parameters on Liquid-Filled Compartment Structure Defense against Metal Jet. *Materials* 2019, 12, 1809.

Zu, X.D.; Huang, Z.X.; Guan, Z.W.; Yin, X.C.; Zheng, Y.M. Influence of a liquid-filled compartment structure on the incoming shaped charge jet stability. *Def. Technol.* 2021, 17, 571–582.